Variable Admittance Control for Obstacle Separation in Aerial Manipulation

Pedro H. M. Souza, Karl Stol*, and Ishaq Hafez
Department of Mechanical and Mechatronics Engineering, University of Auckland, Auckland 1010, New Zealand

ABSTRACT

This paper presents variable admittance control for elastic obstacle separation using a fully actuated fixed-tilt octorotor aerial manipulator. The vehicle carries a single-actuator spreading mechanism that applies opposing contact forces to separate elastic obstacles while limiting the resultant interaction force on the vehicle. The controller modifies the reference motion using the estimated translational force and yaw moment, while the wrench estimator uses online recursive least-squares (RLS) correction to compensate for unmodeled aerodynamic effects. The admittance parameters vary channel-wise as functions of the estimated wrench component, obstacle distance, and actuator saturation, producing stiff free-flight tracking and compliant contact response without mode switching. An experiment demonstrates bounded vehicle motion during sustained separation of two elastic bars.

1 INTRODUCTION

Aerial manipulation enables unmanned aerial vehicles (UAVs) to perform tasks requiring physical interaction with the environment. Contact inspection, repair, human-UAV interaction, and plant sampling require the vehicle to regulate interaction forces while maintaining stable flight [1, 2, 3, 4]. In agricultural and ecological applications, the target region may be obstructed by branches, twigs, or other elastic obstacles [5, 6]. The vehicle may need to displace these obstacles before inspection or sampling, requiring force regulation and sufficient actuation authority.

Fully actuated multirotors are suitable for aerial physical interaction because they reduce the coupling between translational force generation and attitude regulation. Rashad et al. [7] reviewed fully actuated multirotor concepts, while Ryll et al. [8] and Bodie et al. [9] demonstrated interaction control on platforms capable of regulating interaction forces. Existing designs use active rotor tilting, thrust-vectoring mechanisms, or fixed-tilt rotor layouts [10, 11, 7]. Active rotor-tilting and thrust-vectoring designs increase body-wrench authority, but require additional actuators and more complex control allocation. Fixed-tilt platforms provide a simpler alternative by using canted rotors to generate horizontal thrust components without requiring large roll or pitch angles [12, 13]. A prior flexible-rod contact experiment with the smaller fixed-tilt platform is shown in Fig. 1. However, this simpler configuration comes at the cost of reduced endurance. When contact loads are transmitted through the vehicle, the achievable contact force is bounded by the available horizontal thrust. Elastic obstacle separation, such as separating flexible tree branches, can require large local contact forces while limiting the resultant force transmitted to the UAV. This motivates a spreading mechanism that generates the separation load through opposing contact forces, reducing the horizontal thrust required from the UAV.

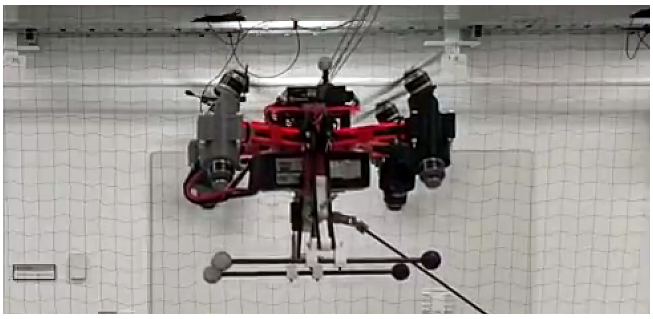


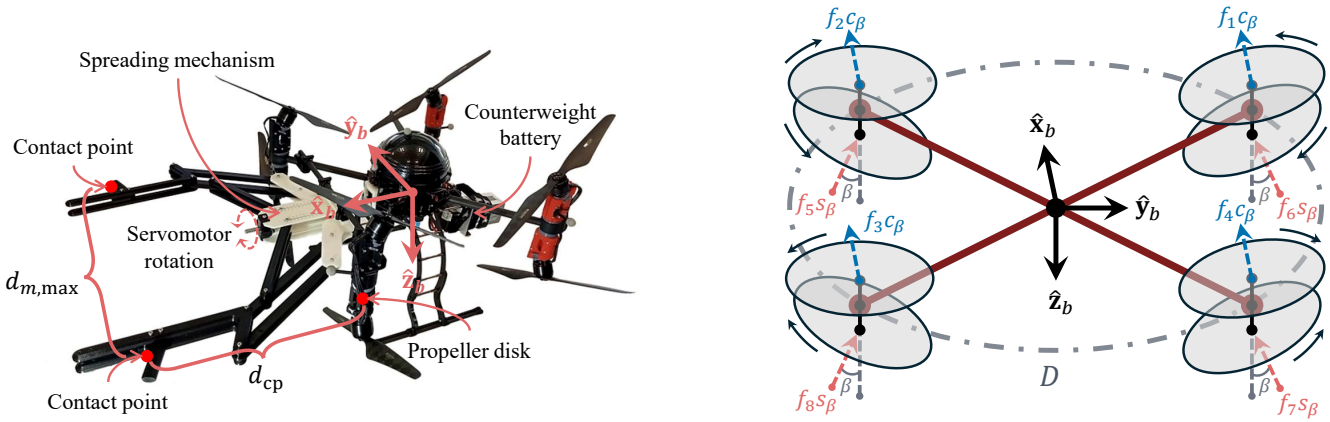
Figure 1: Contact experiment between the smaller fixed-tilt multirotor and a vertical flexible rod [13].

The mechanism increases local contact-force capability, but interaction control remains necessary. Admittance control addresses this problem by mapping the estimated external wrench to reference motion through virtual inertia, damping, and stiffness [4, 14, 15]. In free flight, high virtual stiffness improves reference tracking and disturbance rejection. During contact, excessive virtual stiffness can increase interaction forces and destabilize the coupled vehicle–environment response, while excessive compliance can degrade positioning accuracy. A fixed-admittance controller uses constant virtual parameters in free flight and contact, requiring a compromise between tracking and compliance. Variable admittance instead updates the virtual inertia, damping, and stiffness online, producing stiff free-flight behavior and compliant contact response without mode switching [9, 16, 17].

This paper contributes a task-specific system that integrates variable-admittance control and wrench estimation with an opposing-force spreading mechanism for elastic obstacle separation. The single-actuator mechanism generates

*Email address: k.stol@auckland.ac.nz

http://www.imavs.org/



(a) Spreading mechanism geometry.

(b) Rotor geometry.

Figure 2: FT-X8 geometry: (a) spreading direction $\hat{\mathbf{s}}_b = \hat{\mathbf{y}}_b$ and (b) $c_\beta = \cos\beta$, $s_\beta = \sin\beta$.

opposing local contact forces, while four channel-wise admittance filters vary their virtual inertia and stiffness according to the corresponding estimated wrench component, obstacle distance, and actuator saturation. Online recursive least-squares (RLS) estimation corrects the applied rotor-wrench and gravity-induced moment terms used by the wrench estimator, and the resulting external-wrench estimate drives the translational and yaw admittance channels. The resulting system operates continuously between free flight and contact without explicit mode switching and is evaluated during sustained bilateral spreading.

2 System Overview

The aerial manipulator is a fully actuated fixed-tilt octorotor, denoted FT-X8. The FT-X8 extends the compact fixed-tilt platform used for flexible-cantilever interaction in [12, 13] by incorporating an opposing-force spreading mechanism. Its eight rotors are arranged in four coaxial pairs with a common cant angle β, as shown in Fig. 2. This layout generates body-frame horizontal thrust components and enables lateral translation while maintaining a near-level attitude. The rotor-to-rotor diameter D is approximately 37% larger than that of the platform in [13]. The rotors regulate vehicle motion, while the spreading mechanism supplies the local contact forces required for elastic obstacle separation.

Let $\mathcal{F}_n$ denote the inertial frame and $\mathcal{F}_b$ the body-fixed frame attached to the vehicle center of mass. The inertial frame follows the North-East-Down (NED) convention, with $\hat{\mathbf{z}}_n = [\,0 \;\; 0 \;\; 1\,]^\top$ pointing downward. The body-frame unit vectors $\hat{\mathbf{x}}_b$, $\hat{\mathbf{y}}_b$, and $\hat{\mathbf{z}}_b$ are shown in Fig. 2. The vehicle position and attitude are $\mathbf{p}_n(t) := [\,x_n(t) \;\; y_n(t) \;\; z_n(t)\,]^\top$ and $\boldsymbol{\eta}(t) := [\,\phi(t) \;\; \theta(t) \;\; \psi(t)\,]^\top$, where $\boldsymbol{\eta}$ follows the ZYX Euler convention. The rotation matrix $\mathbf{R}_b^n(t) \in SO(3)$ maps vectors from $\mathcal{F}_b$ to $\mathcal{F}_n$, with $\mathbf{R}_n^b(t) := (\mathbf{R}_b^n(t))^\top$. The body-frame linear and angular velocities are $\mathbf{v}_b(t) := [\,v_{x,b}(t) \;\; v_{y,b}(t) \;\; v_{z,b}(t)\,]^\top$ and $\boldsymbol{\omega}_b(t) := [\,p(t) \;\; q(t) \;\; r(t)\,]^\top$. The external wrench is $\mathbf{w}_{e,b}(t) := [\,\mathbf{f}_{e,b}^\top(t) \;\; \boldsymbol{\tau}_{e,b}^\top(t)\,]^\top$.

The rigid-body dynamics and fixed-tilt rotor model follow [12, 13]. Let $m > 0$, $g > 0$, and $\mathbf{J} \succ 0$ denote the total mass, gravitational acceleration, and inertia matrix. The rotor-generated body wrench is $\mathbf{w}_b(t) := [\,\mathbf{f}_b^\top(t) \;\; \mathbf{m}_b^\top(t)\,]^\top$. With the rotor thrust vector $\mathbf{f}_r(t) := [\,f_1(t) \;\cdots\; f_8(t)\,]^\top$, the allocation model is $\mathbf{w}_b(t) = \boldsymbol{\Lambda}\mathbf{f}_r(t)$, where $\boldsymbol{\Lambda} \in \mathbb{R}^{6\times 8}$. Since $\mathrm{rank}(\boldsymbol{\Lambda}) = 6$, the vehicle is fully actuated.

The spreading mechanism is mounted on the front arms and driven by a Dynamixel MX-64 servomotor through a lead-screw linkage. It produces approximately parallel motion at the two contact points during actuation. As shown in Fig. 2a, the maximum contact-point separation is denoted $d_{m,\max}$, and the contact-point clearance d_{cp} is the minimum distance from either contact point to the nearest propeller disk. The 6S LiPo battery counterweights the manipulator to reduce the center-of-mass offset.

Let $\hat{\mathbf{s}}_b := \hat{\mathbf{y}}_b$ denote the body-frame spreading direction. For the two obstacle contacts, the contact forces are

$$\mathbf{f}_{c,1,b} = F_1\hat{\mathbf{s}}_b, \qquad \mathbf{f}_{c,2,b} = -F_2\hat{\mathbf{s}}_b,$$

where $F_1, F_2 \geq 0$ are the contact force magnitudes. The reaction force transmitted to the vehicle is

$$\mathbf{f}_{m,b} = -\mathbf{f}_{c,1,b} - \mathbf{f}_{c,2,b} = (F_2 - F_1)\hat{\mathbf{s}}_b.$$

For symmetric obstacle separation, the bars have approximately equal stiffness, so $F_1 \approx F_2$. The mechanism therefore applies a pair of opposing local contact forces, producing a small resultant force on the vehicle. The variable-admittance channels use an estimate of the resultant external wrench, $\hat{\mathbf{w}}_{e,b}$, rather than the individual contact forces F_1 and F_2, because only their net effect enters the vehicle dynamics. For unequal bar stiffness, $F_1 \neq F_2$, so $\mathbf{f}_{m,b} \neq \mathbf{0}$. Because the contact points are offset from the vehicle center of mass, this imbalance may also produce an external moment about

http://www.imavs.org/

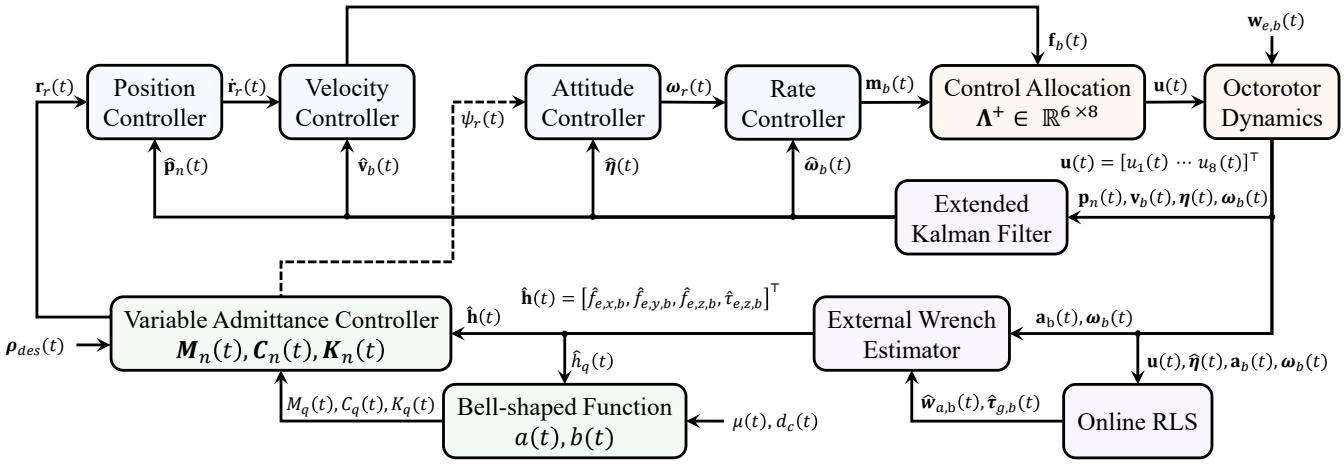


Figure 3: Variable admittance control architecture.

Table 1: FT-X8 with spreading mechanism parameters.

Parameter	Value
Motor model	T-Motor U5-400
Propeller	CF NS16x5.4
Rotor cant angle, β	30°
Rotor-to-rotor diameter, D	0.625 m
Total mass, m	7.1 kg
Manipulator mass	1.8 kg
Maximum horizontal thrust	19.7 N
Manipulator maximum load	115 N
Maximum separation, $d_{m,\max}$	0.463 m
Contact-point clearance, d_{cp}	0.225 m

$\hat{\mathbf{z}}_b$. The estimated force and yaw moment drive the translational and yaw admittance channels, respectively. Performance under this imbalance depends on wrench-estimation accuracy and available body-wrench authority. The attainable local contact force is constrained primarily by the manipulator maximum load, whereas the available horizontal thrust constrains the resultant force transmitted to the vehicle.

The vehicle pose is measured by a Vicon motion-capture system. An offboard MATLAB/Simulink interface exchanges position setpoints and pose measurements with a Pixhawk 4 running the PX4 flight stack [18] over MAVLink. The spreading mechanism is commanded separately, while PX4 tracks the admittance-shaped reference.

3 VARIABLE ADMITTANCE CONTROL

The outer admittance loop modifies the desired reference to generate an admittance-shaped reference, which is tracked by the inner PX4 flight controller, as shown in Fig. 3. The desired translational reference is expressed in $\mathcal{F}_b$ as

$$\mathbf{r}_{\mathrm{des}}(t) := [\, x_{\mathrm{des}}(t) \;\; y_{\mathrm{des}}(t) \;\; z_{\mathrm{des}}(t) \,]^\top,$$

with desired yaw angle $\psi_{\mathrm{des}}(t)$. The admittance loop generates the compliant translational reference

$$\mathbf{r}_r(t) := [\, x_r(t) \;\; y_r(t) \;\; z_r(t) \,]^\top$$

and yaw reference $\psi_r(t)$. The combined references are

$$\boldsymbol{\rho}_{\mathrm{des}}(t) := [\, \mathbf{r}_{\mathrm{des}}^\top(t) \;\; \psi_{\mathrm{des}}(t) \,]^\top, \quad \boldsymbol{\rho}_r(t) := [\, \mathbf{r}_r^\top(t) \;\; \psi_r(t) \,]^\top.$$

The admittance loop uses the body-frame external wrench estimate $\hat{\mathbf{w}}_{e,b}(t) := [\, \hat{\mathbf{f}}_{e,b}^\top(t) \;\; \hat{\boldsymbol{\tau}}_{e,b}^\top(t) \,]^\top$. This estimate is obtained by combining an acceleration-based force observer and an angular-momentum-based external-moment observer using accelerometer and gyroscope measurements and the rotor-generated wrench, without requiring a force/torque sensor. The PX4 state estimator provides the vehicle-state inputs to these observers. The force and moment observers compute $\hat{\mathbf{w}}_{e,b}(t)$ using RLS-corrected model terms. The specific force measured by the accelerometer, expressed in $\mathcal{F}_b$, is

$$\mathbf{a}_b(t) = \mathbf{R}_n^b(t)\big(\ddot{\mathbf{p}}_n(t) - g\hat{\mathbf{z}}_n\big).$$

Let $\hat{\mathbf{w}}_{a,b}(t) := [\, \hat{\mathbf{f}}_{a,b}^\top(t) \;\; \hat{\boldsymbol{\tau}}_{a,b}^\top(t) \,]^\top$ denote the RLS-corrected applied rotor wrench, and let $\hat{\boldsymbol{\tau}}_{g,b}(t)$ denote the moment from the estimated center-of-mass offset. The body-frame external force and moment observers are

$$\hat{\mathbf{f}}_{e,b}(t) = \mathbf{K}_f \int_0^t \Big(m\mathbf{a}_b(\sigma) - \hat{\mathbf{f}}_{a,b}(\sigma) - \hat{\mathbf{f}}_{e,b}(\sigma) \Big) d\sigma, \quad (1)$$

$$\hat{\boldsymbol{\tau}}_{e,b}(t) = \mathbf{K}_\tau \Bigg[\mathbf{J}\boldsymbol{\omega}_b(t) - \int_0^t \Big(\mathbf{J}\boldsymbol{\omega}_b(\sigma) \times \boldsymbol{\omega}_b(\sigma) + \hat{\boldsymbol{\tau}}_{g,b}(\sigma) + \hat{\boldsymbol{\tau}}_{a,b}(\sigma) - \hat{\boldsymbol{\tau}}_{e,b}(\sigma) \Big) d\sigma \Bigg]. \quad (2)$$

Here, $\mathbf{K}_f \succ 0$ and $\mathbf{K}_\tau \succ 0$ are force and moment estimator gain matrices. A small dead zone is applied to the estimated

http://www.imavs.org/

http://www.imavs.org/

wrench components to suppress sensor-noise-induced residuals near the zero-wrench condition.

The RLS block updates estimates of the constant parameters used in $\hat{\mathbf{w}}_{a,b}(t)$ and $\hat{\boldsymbol{\tau}}_{g,b}(t)$ [19]. It corrects the rotor-wrench model for aerodynamic interference in the canted coaxial pairs and the center-of-mass offset introduced by the spreading mechanism. The RLS update corrects only the rotor-wrench and gravity-induced moment terms online. The estimator is initialized from free-flight data and uses actuator commands and onboard inertial measurements. The corrected terms are used in the wrench estimator before the residual external wrench is computed. The RLS block does not estimate contact forces directly or change the admittance law.

For the admittance law, the full wrench estimate is reduced to the translational force components and the body z-axis moment. The four-channel admittance input is

$$\hat{\mathbf{h}}(t) := [\, \hat{f}_{e,x,b}(t) \;\; \hat{f}_{e,y,b}(t) \;\; \hat{f}_{e,z,b}(t) \;\; \hat{\tau}_{e,z,b}(t) \,]^\top,$$

where $\hat{\tau}_{e,z,b}(t)$ is the estimated moment about $\hat{\mathbf{z}}_b$. Roll and pitch remain regulated by the inner attitude controller and are therefore excluded from the admittance input.

The virtual inertia, damping, and stiffness matrices are

$$\mathbf{M}_n(t) = \operatorname{diag}\big(M_x(t), M_y(t), M_z(t), M_\psi(t)\big),$$
$$\mathbf{C}_n(t) = \operatorname{diag}\big(C_x(t), C_y(t), C_z(t), C_\psi(t)\big),$$
$$\mathbf{K}_n(t) = \operatorname{diag}\big(K_x(t), K_y(t), K_z(t), K_\psi(t)\big).$$

The diagonal structure gives four decoupled admittance filters for the translational components in $\mathcal{F}_b$ and yaw. For each channel $q \in \mathcal{Q} := \{x, y, z, \psi\}$, the scalar admittance input is

$$\hat{h}_q(t) := \begin{cases} \hat{f}_{e,q,b}(t), & q \in \{x, y, z\}, \\ \hat{\tau}_{e,z,b}(t), & q = \psi. \end{cases}$$

The channel-wise admittance equation for q is

$$M_q(t)\big(\ddot{\rho}_{r,q}(t) - \ddot{\rho}_{\mathrm{des},q}(t)\big) + C_q(t)\big(\dot{\rho}_{r,q}(t) - \dot{\rho}_{\mathrm{des},q}(t)\big) + K_q(t)\big(\rho_{r,q}(t) - \rho_{\mathrm{des},q}(t)\big) = \hat{h}_q(t).$$

Each bell-shaped law uses the scalar channel input $\hat{h}_q(t)$, not the full vector $\hat{\mathbf{h}}(t)$. The inertia and stiffness are defined by generalized bell-shaped functions [20]. For each $q \in \mathcal{Q}$,

$$M_q(t) = M_{q,\min} + \frac{M_{q,\max} - M_{q,\min}}{1 + \left|\frac{\hat{h}_q(t)}{a(t)}\right|^{2b(t)}}, \tag{3}$$

and

$$K_q(t) = K_{q,\min} + \frac{K_{q,\max} - K_{q,\min}}{1 + \left|\frac{\hat{h}_q(t)}{a(t)}\right|^{2b(t)}}. \tag{4}$$

The bounds satisfy $0 < M_{q,\min} < M_{q,\max}$ and $0 < K_{q,\min} < K_{q,\max}$. For small wrench components, (3) and (4) remain near $M_{q,\max}$ and $K_{q,\max}$, producing stiff tracking and disturbance rejection. For larger wrench components, $M_q(t)$ and $K_q(t)$ approach $M_{q,\min}$ and $K_{q,\min}$, increasing compliance during contact. The damping coefficient is set to

$$C_q(t) = 2\sqrt{M_q(t) K_q(t)}, \qquad q \in \mathcal{Q},$$

which sets each channel damping ratio to one.

The distance to the obstacles and actuator saturation modify the bell-shaped admittance law. Let $d_c(t) \geq 0$ denote the minimum distance from the manipulator contact points to the two elastic obstacles, with $d_c(t) = 0$ during contact. The distance-dependent shape parameter is

$$b(t) = b_1 - b_2 \exp\left(-\frac{4 d_c(t)}{b_3}\right), \tag{5}$$

where $b_1 > b_2 > 0$ and $b_3 > 0$. When the vehicle is far from the obstacles, $d_c(t)$ is large and $b(t) \approx b_1$, producing a sharper transition that keeps the virtual inertia and stiffness near their maximum values for small estimated wrench components. As the vehicle approaches contact, $b(t)$ decreases toward $b_1 - b_2$, and the smoother transition makes the virtual inertia and stiffness decrease at lower wrench magnitudes.

The bell-shaped law is also adjusted by actuator saturation so that compliance increases near actuator limits. Let $\mathbf{u}(t) := [\, u_1(t) \;\cdots\; u_8(t) \,]^\top \in [u_{\min}, u_{\max}]^8$ denote the motor pulse-width-modulation (PWM) command vector, where $u_{\min} = 1000\ \mu$s, $u_{\max} = 2000\ \mu$s, and $u_0 := (u_{\min} + u_{\max})/2 = 1500\ \mu$s. The raw saturation factor is

$$\mu_r(t) = \frac{\|\mathbf{u}(t) - u_0 \mathbf{1}_8\|_\infty}{u_{\max} - u_0}, \tag{6}$$

so that $\mu_r(t) = 0$ when all commands are centered at $1500\ \mu$s and $\mu_r(t) = 1$ when at least one motor reaches a saturation limit. A first-order low-pass filter is applied to $\mu_r(t)$ to obtain the filtered saturation factor $\mu(t) \in [0, 1]$ and avoid rapid parameter variation. The bell-width parameter is

$$a(t) = a_1 - \mu(t), \tag{7}$$

where $a_1 > 1$ sets the maximum bell width. As actuator saturation is approached, $\mu(t)$ increases and $a(t)$ decreases, so $M_q(t)$ and $K_q(t)$ decrease at smaller wrench magnitudes, increasing compliance near actuator limits.

Equations (3)–(7) define the admittance parameters as functions of the estimated wrench component $\hat{h}_q(t)$, obstacle distance $d_c(t)$, and filtered saturation factor $\mu(t)$. Thus, the same admittance law applies in free flight and contact, without explicit switching between modes.

Table 2 lists the admittance bounds for the translation axes (x_b, y_b, z_b) and yaw ψ, the bell-shaped law parameters, and the saturation-filter time constant. The bounds were selected so that $M_q(t)$ and $K_q(t)$ remain high in free flight and decrease during contact and near actuator saturation.

Table 2: Admittance parameters for obstacle separation.

Parameter	Translation axes	Yaw
$M_{\min}$	1 kg	10 kg m^2
$M_{\max}$	10 kg	100 kg m^2
$K_{\min}$	25 N/m	8 N m/rad
$K_{\max}$	50 N/m	10 N m/rad
Bell-shaped law parameters $a_1 = 2.5$, $b_1 = 5$, $b_2 = 3.5$, $b_3 = 2$ m		
Saturation-filter time constant $\tau_\mu = 5$ s		

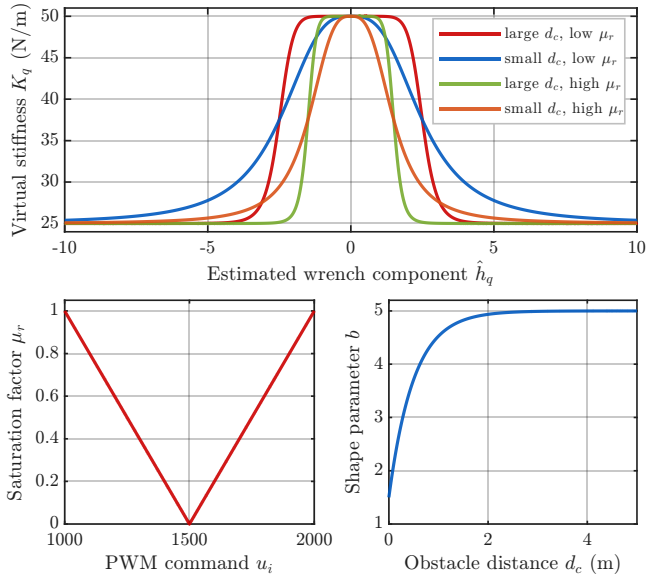


Figure 4: Effect of $a(t)$ and $b(t)$ on the stiffness law.

Fig. 4 illustrates the stiffness variation in (4) using the translational stiffness bounds from Table 2. The four curves correspond to combinations of obstacle distance and actuator saturation factor. For large d_c, $b \approx b_1$, while near contact $b \approx b_1 - b_2$. Low saturation gives $\mu \approx 0$ and $a \approx a_1$, while high saturation increases μ and reduces a. A larger a keeps K_q near $K_{\max}$ over a wider range of $|\hat{h}_q|$, so the drop toward $K_{\min}$ occurs at larger wrench magnitudes. A larger b keeps the response stiff for small wrench magnitudes and makes the transition to the compliant region sharper. The inertia law in (3) follows the same dependence on $\hat{h}_q(t)$, $a(t)$, and $b(t)$.

4 EXPERIMENTAL VALIDATION

The variable admittance controller is evaluated on the FT-X8 aerial manipulator during elastic obstacle separation. The experiment uses the equal-stiffness test rig shown in Fig. 5, where two vertical bars are restrained by elastic bands to emulate elastic obstacles. As the spreading mechanism opens, it contacts and separates the two bars while the vehicle remains under position control. This setup evaluates whether the controller maintains bounded vehicle motion while the mechanism applies large local contact forces during sustained bilateral contact.

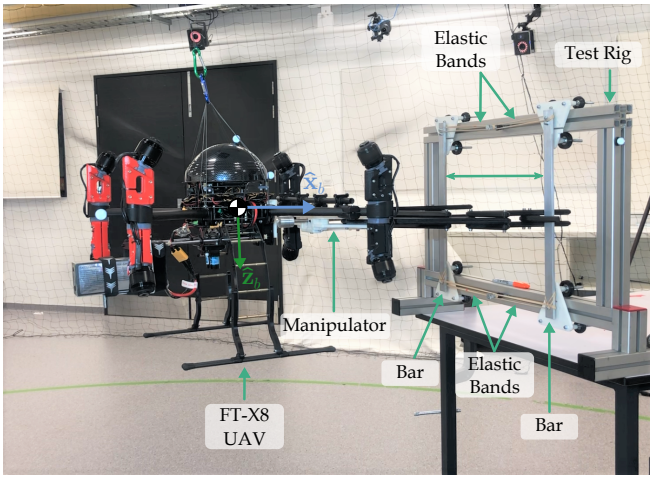


Figure 5: Experimental setup for elastic obstacle separation.

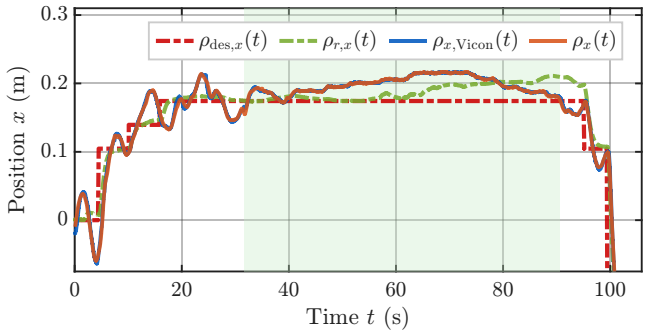
The vehicle is commanded to hover with the admittance controller active and then approach the center of the test rig until the spreading mechanism is positioned between the bars and the vehicle body-frame $\hat{\mathbf{y}}_b$ axis is aligned with the test-rig normal. After the mechanism is inserted between the bars, the servomotor drives the spreading mechanism gradually through its opening and closing motion, with both contact points remaining in contact with the elastic bars. The measured stiffness of each bar along $\hat{\mathbf{y}}_b$ is 387 N/m. Based on this stiffness and the full-opening displacement, full opening corresponds to an inferred local force of nearly 88 N per bar. This inferred local force is 4.5 times the maximum horizontal thrust listed in Table 1.

In Figs. 6 and 7, the green shaded region denotes the bilateral spreading phase, during which both contact points remain in contact with the bars as the mechanism opens and closes. The unshaded portions correspond to vehicle positioning before and after bilateral contact. In Fig. 6, for each plotted component $q \in \{x, y, z, \psi\}$, the desired reference is denoted by $\rho_{\mathrm{des},q}$, the admittance-shaped reference by $\rho_{r,q}$, the PX4 estimate by ρ_q, and the Vicon measurement by $\rho_{q,\mathrm{Vicon}}$.

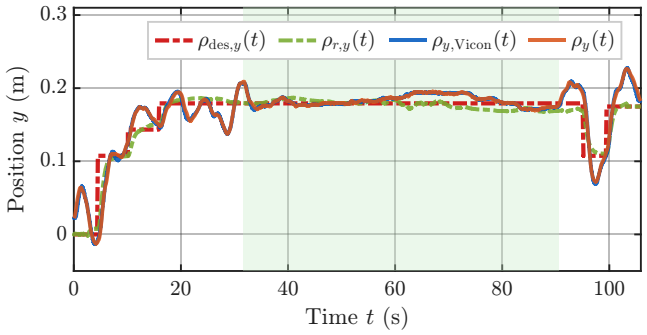
Fig. 6 shows the vehicle motion during spreading. The PX4 estimate and Vicon measurement follow the same horizontal-motion trend. During bilateral spreading, the admittance-shaped reference intentionally deviates from the desired reference because the variable admittance law modifies the reference in response to the estimated interaction wrench instead of enforcing rigid tracking of the desired reference. The horizontal reference deviations persist throughout the bilateral phase, indicating sustained compliance rather than a short contact transient. The desired vertical reference remains nearly constant, while the Vicon measurement varies by 0.041 m peak to peak over the interval shown.

http://www.imavs.org/

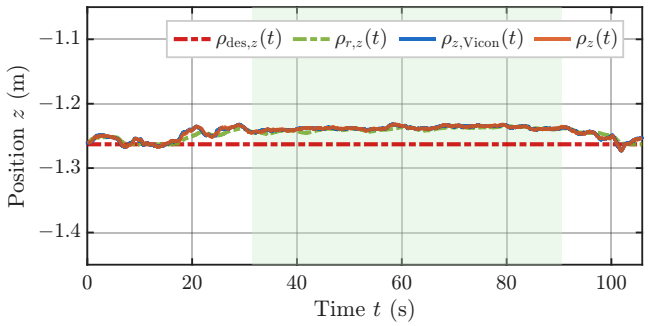
http://www.imavs.org/



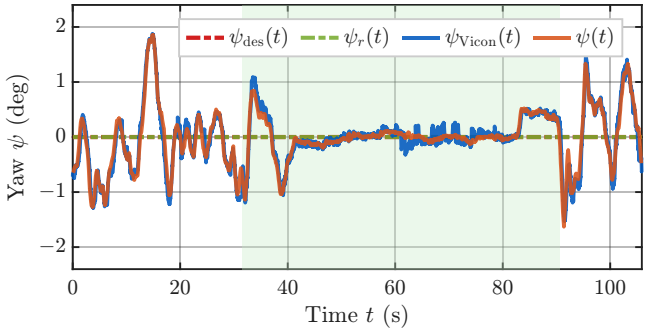
(a) x response.



(b) y response.

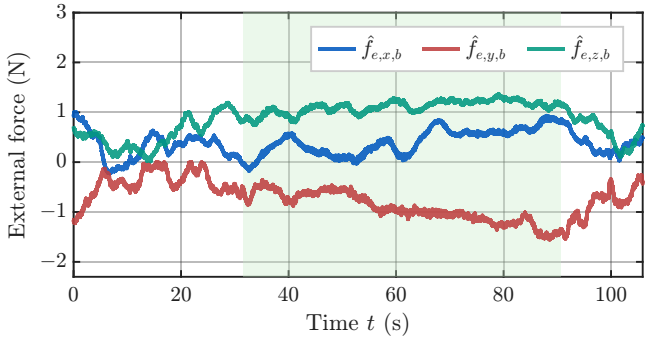


(c) z response.

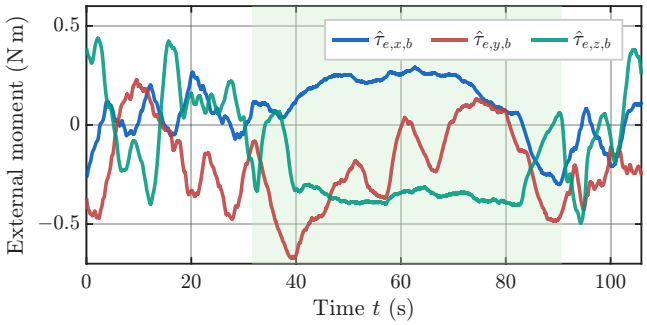


(d) Yaw response.

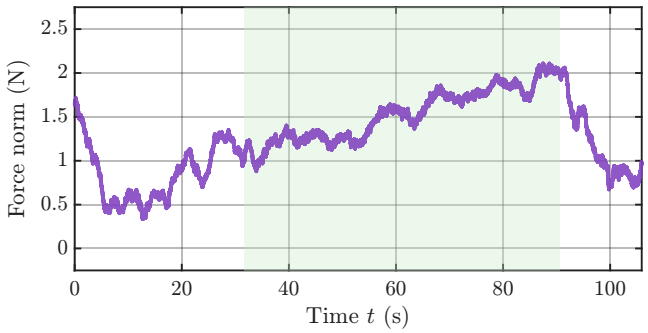
Figure 6: Vehicle motion during the spreading experiment. The shaded region marks the bilateral spreading phase.



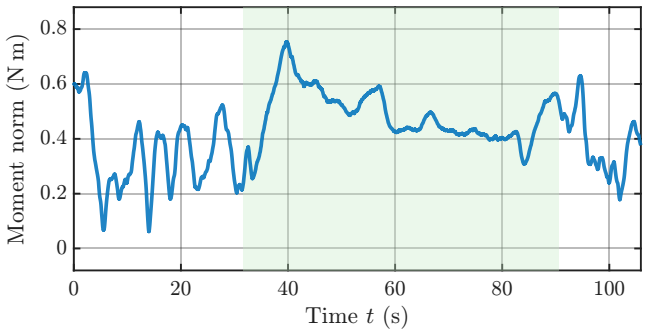
(a) External force components $\hat{f}_{e,q,b}$, $q \in \{x, y, z\}$.



(b) External moment components $\hat{\tau}_{e,q,b}$, $q \in \{x, y, z\}$.



(c) External force norm $\|\hat{\mathbf{f}}_{e,b}\|$.



(d) External moment norm $\|\hat{\boldsymbol{\tau}}_{e,b}\|$.

Figure 7: RLS-corrected external wrench estimate during the spreading experiment, expressed in the body frame. The component plots show the dominant interaction directions, while the norms summarize the force and moment magnitudes.

http://www.imavs.org/

The root-mean-square (RMS) yaw-tracking error relative to ψ_r over the bilateral spreading phase was 0.293° for the PX4 estimate ψ and 0.310° for the Vicon measurement ψ_{Vicon}. The corresponding maximum absolute yaw-tracking errors were 1.14° and 1.19°, respectively. During bilateral spreading, the maximum raw saturation factor computed from the eight motor PWM commands using (6) was $\mu_{r,\max} = 0.334$, corresponding to a minimum PWM margin of $\Delta u_{\min} = 333$ μs to the nearest saturation limit. The motor PWM commands remained within 1422–1667 μs during this phase, and no motor command reached the 1000 or 2000 μs limits. The response therefore shows bounded vehicle motion while retaining actuator authority during separation.

Fig. 7 shows the RLS-corrected external wrench estimate. The estimated force components and force norm increase during bilateral spreading and decrease after bilateral contact ends, indicating sustained obstacle interaction. The dominant force component is along the body $\hat{\mathbf{y}}_b$ axis, which is the spreading direction $\hat{\mathbf{s}}_b$, and has a peak magnitude of approximately 1.56 N. The peak absolute force components are approximately 0.93 N, 1.56 N, and 1.37 N along the $\hat{\mathbf{x}}_b$, $\hat{\mathbf{y}}_b$, and $\hat{\mathbf{z}}_b$ axes, respectively, and the peak force norm is approximately 2.11 N. The peak absolute moment components are approximately 0.30 N m, 0.67 N m, and 0.41 N m along the $\hat{\mathbf{x}}_b$, $\hat{\mathbf{y}}_b$, and $\hat{\mathbf{z}}_b$ axes, respectively, with a peak moment norm of approximately 0.754 N m.

The key quantitative result is the scale separation between the local obstacle-separation force and the resultant force transmitted to the vehicle. The inferred local force at full opening is nearly 88 N per bar, whereas the peak resultant force estimated at the vehicle is 2.11 N, corresponding to a local-to-resultant force ratio of 40. This occurs because opposing contact forces make the resultant force on the vehicle depend primarily on force imbalance rather than individual contact-force magnitudes. The spreading mechanism supplies the local force needed to displace the obstacles, and the variable admittance controller modifies the reference during interaction so that the vehicle remains bounded instead of rigidly tracking the desired reference.

5 CONCLUSION

This paper presented variable admittance control for elastic obstacle separation with a fully actuated fixed-tilt aerial manipulator. The FT-X8 uses a single-actuator spreading mechanism to apply opposing contact forces while the rotors regulate vehicle motion. The admittance law varies the virtual inertia and stiffness as functions of the estimated wrench component, obstacle distance, and actuator saturation, producing stiff free-flight tracking and compliant contact response without mode switching. In the spreading experiment, the inferred local obstacle-separation force was 40 times the peak resultant force estimated at the vehicle. This result demonstrates large local separation forces with bounded vehicle motion during contact.

ACKNOWLEDGEMENTS

The research was conducted as part of "Enabling Unmanned Aerial Vehicles (drones) to Use Tools in Complex Dynamic Environments UOCX2104", funded by the New Zealand Ministry of Business, Innovation and Employment.

REFERENCES

[1] Anibal Ollero, Marco Tognon, Alejandro Suarez, Dongjun Lee, and Antonio Franchi. Past, present, and future of aerial robotic manipulators. *IEEE Transactions on Robotics*, 38(1):626–645, 2022.

[2] Fabio Ruggiero, Vincenzo Lippiello, and Anibal Ollero. Aerial manipulation: A literature review. *IEEE Robotics and Automation Letters*, 3(3):1957–1964, 2018.

[3] Pisak Chermprayong, Ketao Zhang, Feng Xiao, and Mirko Kovac. An integrated delta manipulator for aerial repair: A new aerial robotic system. *IEEE Robotics & Automation Magazine*, 26(1):54–66, 2019.

[4] Federico Augugliaro and Raffaello D'Andrea. Admittance control for physical human-quadrocopter interaction. In *2013 European Control Conference (ECC)*, pages 1805–1810, 2013.

[5] James R. Kutia, Karl A. Stol, and Weiliang Xu. Aerial manipulator interactions with trees for canopy sampling. *IEEE/ASME Transactions on Mechatronics*, 23(4):1740–1749, 2018.

[6] Hughes La Vigne, Guillaume Charron, Julien Rachiele-Tremblay, David Rancourt, Ben Nyberg, and Alexis Lussier Desbiens. Collecting critically endangered cliff plants using a drone-based sampling manipulator. *Scientific Reports*, 12(1):14827, 2022.

[7] Ramy Rashad, Jelmer Goerres, Ronald G. K. M. Aarts, Johan B. C. Engelen, and Stefano Stramigioli. Fully actuated multirotor uavs: A literature review. *IEEE Robotics & Automation Magazine*, 27(3):97–107, 2020.

[8] Markus Ryll, Giuseppe Muscio, Francesco Pierri, Elisabetta Cataldi, Gianluca Antonelli, Fabrizio Caccavale, Davide Bicego, and Antonio Franchi. 6d interaction control with aerial robots: The flying end-effector paradigm. *The International Journal of Robotics Research*, 38(9):1045–1062, 2019.

[9] Karen Bodie, Maximilian Brunner, Michael Pantic, Stefan Walser, Patrick Pfändler, Ueli Angst, Roland Siegwart, and Juan Nieto. Active interaction force control for contact-based inspection with a fully actuated aerial vehicle. *IEEE Transactions on Robotics*, 37(3):709–722, 2021.

[10] Chao Ding and Lu Lu. A tilting-rotor unmanned aerial vehicle for enhanced aerial locomotion and manipulation capabilities: Design, control, and applications. *IEEE/ASME Transactions on Mechatronics*, 26(4):2237–2248, 2021.

[11] Moju Zhao, Kei Nagato, Kei Okada, Masayuki Inaba, and Masaru Nakao. Forceful valve manipulation with arbitrary direction by articulated aerial robot equipped with thrust vectoring apparatus. *IEEE Robotics and Automation Letters*, 7(2):4893–4900, 2022.

[12] Pedro H. M. Souza and Karl Stol. Analysis and design of a novel fully-actuated compact multirotor. In *Proceedings of the Australasian Conference on Robotics and Automation*, 2021.

[13] Pedro Henrique Mendes Souza and Karl Stol. Constrained dynamics of an aerial manipulator interacting with flexible cantilever beams. *IEEE/ASME Transactions on Mechatronics*, 28(2):967–975, 2023.

[14] A. Q. L. Keemink, H. van der Kooij, and A. H. A. Stienen. Admittance control for physical human-robot interaction. *The International Journal of Robotics Research*, 37(11):1421–1444, 2018.

[15] Teodor Tomić, Christian Ott, and Sami Haddadin. External wrench estimation, collision detection, and reflex reaction for flying robots. *IEEE Transactions on Robotics*, 33(6):1467–1482, 2017.

[16] Gwang Kang, Hwan-Soo Oh, Jeong-Ki Seo, Uikyum Kim, and Hyouk Ryeol Choi. Variable admittance control of robot manipulators based on human intention. *IEEE/ASME Transactions on Mechatronics*, 24(3):1023–1032, 2019.

[17] Hui-Yu Li, Ishara Paranawithana, Liangjing Yang, T. S. K. Lim, Shaohui Foong, F. C. Ng, and U-Xuan Tan. Stable and compliant motion of physical human-robot interaction coupled with a moving environment using variable admittance and adaptive control. *IEEE Robotics and Automation Letters*, 3(3):2493–2500, 2018.

[18] PX4 Development Team. PX4 Autopilot Software. `https://github.com/PX4/PX4-Autopilot`. Accessed: 2026-05-15.

[19] Dan Simon. *Optimal State Estimation: Kalman, H Infinity, and Nonlinear Approaches*. Wiley-Interscience, Hoboken, NJ, USA, 2006.

[20] Jyh-Shing Roger Jang. ANFIS: Adaptive-network-based fuzzy inference system. *IEEE Transactions on Systems, Man, and Cybernetics*, 23(3):665–685, 1993.

http://www.imavs.org/